



## **An integrated and homogenized global surface solar radiation dataset and its reconstruction based on an artificial intelligence approach**

5 Boyang Jiao<sup>1,#</sup>, Yucheng Su<sup>2</sup>, Qingxiang Li<sup>\*1,#</sup>, Veronica Manara<sup>3</sup>, Martin Wild<sup>4</sup>

<sup>1</sup>School of Atmospheric Sciences, Sun Yat-sen University, and Key Laboratory of Tropical Atmosphere–Ocean System, Ministry of Education, Zhuhai 519082, China

<sup>2</sup>Meteorological Bureau of Zhuhai, Zhuhai 519082, China

10 <sup>3</sup>Department of Environmental Science and Policy, Università degli Studi di Milano, via Celoria 10, 20133, Milano, Italy

<sup>4</sup>Institute for Atmospheric and Climate Science, ETH Zurich, Zurich, Switzerland

<sup>#</sup>Southern Laboratory of Ocean Science and Engineering (Guangdong Zhuhai), Zhuhai 519082, China

*Correspondence to:* Qingxiang Li ([liqingx5@mail.sysu.edu.cn](mailto:liqingx5@mail.sysu.edu.cn))

15



## Abstract

Surface solar radiation (SSR) is an essential factor in the flow of surface energy, enabling accurate capturing of long-term climate change and understanding the energy balance of Earth's atmosphere system. However, the long-term trend estimation of SSR is subjected to significant uncertainties due to the temporal inhomogeneity and the uneven spatial distribution of the *in-situ* observations. This paper develops an observational integrated and homogenized global-terrestrial (except for Antarctica) 20 stational SSR dataset (SSRIH<sub>station</sub>) by integrating all available SSR observations, including the existing homogenized SSR results. The series are then interpolated in order to obtain a 5°×5° resolution gridded dataset (SSRIH<sub>grid</sub>). On this basis, we further reconstruct a long-term (1955-2018) global land (except for 25 Antarctica) SSR anomalies dataset with a 5°×2.5° resolution (SSRIH<sub>20CR</sub>) by training improved partial convolutional neural network deep learning methods based on the reanalysis 20CRv3. Based on this, we analysed the global land (except for Antarctica) /regional scale SSR trends and spatiotemporal variations: the reconstruction results reflect the distribution of SSR anomalies and have high reliability in filling and reconstructing the missing values. At the global land (except for Antarctica) scale, the decreasing trend 30 of the SSRIH<sub>20CR</sub> (-1.276±0.205 W/m<sup>2</sup> per decade) is slightly smaller than the trend of the SSRIH<sub>grid</sub> (-1.776±0.230 W/m<sup>2</sup> per decade) from 1955 to 1991. The trend of SSRIH<sub>20CR</sub> (0.697±0.359 W/m<sup>2</sup> per decade) from 1991 to 2018 is also marginally lower than that of the SSRIH<sub>grid</sub> (0.851±0.410 W/m<sup>2</sup> per decade). At the regional scale, the difference between the SSRIH<sub>20CR</sub> and SSRIH<sub>grid</sub> is more significant in years and areas with insufficient coverage. Asia, Africa, Europe and North America cause the global 35 dimming of the SSRIH<sub>20CR</sub>, while Europe and North America drive the global brightening of the SSRIH<sub>20CR</sub>. Spatial sampling inadequacies have largely contributed to a bias in the long-term variation of global/regional SSR. This paper's homogenized gridded dataset and the Artificial Intelligence reconstruction gridded dataset (Jiao and Li, 2023) are all available at <https://doi.org/10.6084/m9.figshare.21625079.v1>.

40



## 1 Introduction

Energy flows at the Earth's surface play an essential role in climate change and human activity and link to physical processes such as global warming, glacier retreating, hydrological cycle, and carbon budget (Hoskins and Valdes, 1990; Peixoto et al., 1992; Trenberth and Fasullo, 2013; Wild, 2012). As a critical  
45 factor characterizing surface energy flows, Surface Solar Radiation (SSR) largely determines the climatic conditions and ecological environment in which we live. Therefore, a more accurate and comprehensive analysis of the SSR fluxes will help better understand the Earth's atmospheric system. *In-situ* observations provide the most accurate baseline data for measuring SSR. They allowed for the first time the detection of decadal changes in SSR known as “dimming and brightening” (Wild et al., 2005),  
50 especially considering that they cover a longer period concerning another type of data like for example satellite data (Pfeifroth et al., 2018) even if observational data often have uneven distribution and missing data with respect to the satellite data, especially in areas with complex orography (Manara et al., 2020).

The sources of *in-situ* SSR observations are mainly collected from the Global Energy Balance Archive (GEBA) (Wild et al., 2017) and the World Radiation Data Centre (WRDC) (Tsvetkov et al., 1995).  
55 Furthermore, other SSR station series are obtained from the high quality Baseline Surface Radiation Network (BSRN) (Driemel et al., 2018) and the data centres of individual national hydrometeorological services. However, two issues still need to be addressed: 1) the inhomogeneity of station data resulting from station relocations and instrumentation changes severely impacts the climate change assessment. For the regions with a relatively high density of stations, like Europe (Manara et al., 2019; Manara et al.,  
60 2016; Sanchez-Lorenzo et al., 2013a; Sanchez-Lorenzo et al., 2015; Sanchez-Lorenzo et al., 2013b), Japan (Ma et al., 2022) and China (Ju et al., 2006; Wang, 2014; Wang et al., 2015; Wang and Wild, 2016; Yang et al., 2018b; You et al., 2013), much previous work has redefined the degree and timing of “dimming and brightening” by addressing the inhomogeneity of the SSR data series. For example, in Spain, the average annual homogenized SSR series has a significant increasing trend (+ 3.9 W/m<sup>2</sup> per  
65 decade) during the 1985–2010 period (Sanchez-Lorenzo et al., 2013a). The period of dimming observed in Italy's homogenized SSR series is not apparent in the 1960s and early 1970s when the raw series (inhomogenized) are taken into account (Manara et al., 2016). The direct measurements of SSR show a level trend from 1961 to 2014 over Japan, while their homogenization series display a decreasing trend (0.8-1.6 W/m<sup>2</sup> per decade) (Ma et al., 2022). In China, homogenization largely eliminated the dramatic



70 non-climatic rise of the early 1990s and also reduced the increasing trend from 1990 to 2016 (Yang et al., 2018b). However, most of the research was still limited to regional scales. 2) The issue of limited spatial sampling of long observational stations and their uneven distribution especially over areas with complex orography. Considerable efforts have been devoted to filling in/interpolating the missing values in climate datasets ("spatial analysis") (Collins, 1996; Erxleben et al., 2002; Scudiero et al., 2016). The  
75 traditional spatial interpolation methods commonly used include Inverse Distance Weighted (Fisher et al., 1993; Shepard, 1968), Kriging (Krige, 1951), Thin-Plate Splines (Bookstein, 1989) et cetera. Since the 1980s, physical parametric interpolation (Feng and Wang, 2021; Tang et al., 2019) and Bayesian fusion schemes (Aguiar et al., 2015) based on multi-source observational data were widely used, when the emergence of highly accurate and relatively precise satellite data. However, the resulting fusion  
80 datasets cover a too short period to investigate their decadal and multi-decadal variations and to study the underlying causes. The rise of deep learning and big data techniques has brought about an explosion of artificial intelligence (AI). Machine learning is increasingly being used in spatial interpolation, such as the spatial reconstruction of surface temperature datasets (Huang et al., 2022; Kadow et al., 2020; Cao et al., 2022), the spatial and temporal reconstruction of turbulence resolution (Fukami et al., 2021), etc.  
85 Furthermore, it shows high accuracy and low uncertainty in reproducing and predicting SSR (Leirvik and Yuan, 2021; Tang et al., 2016; Yang et al., 2018a; Yuan et al., 2021). However, long-term homogenized SSR datasets with global terrestrial coverage have yet to be developed, resulting in significant uncertainties in assessing global SSR variation (Jiao et al., 2022).

Therefore, developing a more homogeneous and comprehensive global long-term SSR climatic dataset  
90 that provides a better benchmark for observational constraints on the global surface energy balance/budget remains a valuable and challenging task. This paper first homogenizes and grids the most extensive collection of available global SSR station observations. Then, the missing grid boxes/years are spatially interpolated using a convolutional neural network (CNN) approach to obtain a globally covered land surface SSR anomalies dataset. Finally, the reconstructed datasets are initially analysed and  
95 evaluated. Thus, the paper is divided into seven main sections. The data resources are introduced in Section 2. Section 3 presents the data homogenization, and the CNN model reconstruction methods. The data homogenization and verification are shown in Section 4. Section 5 gives the AI reconstruction results. Section 6 is the availability of the datasets. Conclusions are provided at the end of the paper.



## 2 Data

100 Nine SSR datasets are collected to derive the global SSR variable. In particular, six datasets contain data from observational stations (Section 2.1): two global ground-based measurement datasets (GEBa, WRDC) and four homogenized products at regional and country levels (Europe, China, Japan and Italy). Three of the adopted datasets are reanalysis data (Section 2.2.1): ERA5, 20th Century Reanalysis version 3 (20CRv3) reanalysis data and the Coupled Model Intercomparison Project Phase 6 (CMIP6) historical simulation output (125). Specifically, the ERA5 data are used to fill the data over oceans and Antarctica (Section 3.2.1), 20CRv3 data and CMIP6 simulations are used for the AI model training (Section 5.1) and reconstruction. All have been listed in Table 1.

### 2.1 In situ observational Data

#### 2.1.1 Global datasets

110 There are two main sources of raw SSR data (see Table 1): the ETH Zurich GEBa with monthly data from 2,445 globally distributed stations, starting from 1922 until 2020, and the WRDC dataset with monthly globally distributed data from 1136 stations since 1964. The first one is available for download at <https://geba.ethz.ch> (Last access: 2022.7. 2). The second one published the first SSR radiation balance data in 1965 and then its publication has been issued four times a year since 1993 and is available for  
115 download at <http://wrdc.mgo.rssi.ru/> (Last access: July 2021).

#### 2.1.2 National (regional) homogenized station datasets

##### 1) Chinese homogenized SSR dataset

The China Meteorological Radiation Fundamental Elements Monthly Value Data Set has been downloaded at <http://www.nmic.cn>. The homogenized SSR dataset in China is released by the National  
120 Meteorological Information Centre (NMIC), China Meteorological Administration (CMA) (Yang, 2016). The data are available for the period between Jan 1950 to Dec 2014, and the follow-up data are extended with raw observations from NMIC. They used the sunshine duration (SSD) data from nearby stations to construct an arguably better reference to identify inhomogeneities in the SSR data. Then, a combined metadata and the maximum penalty t-test (PMT) method was used to detect the change points. Finally,  
125 they were adjusted by a quantile matching (QM) algorithm (Wang and Feng, 2013). The final homogenized SSR station dataset was converted to gridded data using the first difference method (FDM



(Peterson et al., 1998)) and is available for download at <http://www.nmic.cn>. Last Access: September 2022.

#### 2) Japanese homogenized SSR dataset

130 Ma et al. (Ma et al., 2022) released a Japanese SSR homogenized dataset in 2022 spanning the period between 1870 and 2015. First, they homogenized SSD based on PMF (penalized maximal F test) and QM algorithms. They then used the homogenized SSD from the previous step as a reference series, combined with metadata and PMT, to detect change points. Finally, they adjusted the change points by the QM algorithm. For more details on data descriptions, the adopted methodology and downloading  
135 data refer to <https://data.tpsc.ac.cn/en/data/45d73756-3f5a-4d27-82a4-952e268c20e8/>. Last Access: March 2022.

#### 3) European homogenized SSR data

A homogenized dataset of European SSR stations was developed by Sanchez-Lorenzo et al. (Sanchez-Lorenzo et al., 2015) and is currently available as a full public download at  
140 <https://agupubs.onlinelibrary.wiley.com/doi/full/10.1002/2015JD023321>. They selected the 56 longest Central European SSR series available in GEBA dataset with data for the period comprised between 1922 and 2012. They adjusted them to ensure temporal homogeneity homogenizing the data with the Standard Normal Homogeneity Test (Alexandersson, 1986) and the Craddock test (Craddock, 1979).

#### 4) Italian homogenized SSR dataset

145 The Italian homogenized SSR datasets are those published by (Manara et al., 2019; Manara et al., 2016). As candidate stations to use as reference series, they selected the ten series located in the same area of the series to be tested and that series correlate well with the test one. In particular, they tested the change points with the Craddock test (Manara et al., 2017) and when a break is identified by more than one reference series the preceding portion of the series is corrected, leaving the most recent portion  
150 unchanged. In this way, the SSR stations were homogenized, and then the missing values were interpolated.

## 2.2 Other datasets

### 2.2.1 Reanalysis

155 ERA5 can be used to fill in SSR data from the oceans and Antarctica and carry out the global reconstruction, taking into account its high spatial resolution and reliable performance of SSR (Jiao et



al., 2022; Liang et al., 2022). After the reconstruction, we removed the data for the ocean reanalysis and maintain the data only in the land area (except for Antarctica). In addition, two SSR data products (20CRv3, CMIP6) are used to train AI models. These are:

1) ERA5 (space-filling data): ERA5 is the fifth generation of the European Centre for Medium-Range  
160 Forecasting reanalysis product, which currently publishes data from 1950 to the present (Hersbach et al.,  
2020). In addition, ERA5 has an hourly output and an uncertainty estimate from the ensemble. The data  
is based on the Integrated Forecasting Model Cy41r2 run in 2016, which contains a 4D-Var assimilation  
scheme. In ERA5, SSR is obtained from a Rapid Radiation Transfer Model (RRTM) (Mlawer et al.,  
1997). The present study utilizes monthly SSR data for the period 1955-2018 from ERA5 with a  
165 resolution of  $0.25^\circ \times 0.25^\circ$  (last accessed in July 2022). It can be downloaded at  
<https://cds.climate.copernicus.eu>

2) 20CRv3 (data for AI model training): The 20CR Project is an effort led by NOAA's Physical  
Sciences Laboratory and CIRES at the University of Colorado, supported by the Department of Energy,  
to produce reanalysis datasets spanning the entire 20th century and much of the 19th century (Slivinski  
170 et al., 2019). 20CR provides a comprehensive global atmospheric circulation data set from 1850 to 2015.  
Its chief motivation is to provide an observational validation dataset, with quantified uncertainties, for  
assessing climate model simulations of the 20th century. 20CR uses an ensemble filter data assimilation  
method which directly estimates the most likely state of the global atmosphere every three hours and  
estimates the uncertainty in that analysis. The most recent version of this reanalysis, 20CRv3, provides  
175 8-times daily estimates of global tropospheric variability across 75 km grids, spanning 1836 to 2015  
(with an experimental extension from 1806 to 1835). The present study uses monthly SSR data of  
20CRv3 (NOAA/CIRES/DOE 20CR, 80 members) from 1955-2015. The SSR of 20CRv3 has a spatial  
resolution of  $0.7^\circ \times 0.7^\circ$  (Last accessed: May 2022). The download is available at  
<https://portal.nersc.gov/archive/home/projects/incite11/>.

### 180 2.2.2 CMIP6 models output

3) CMIP6 models output (data for AI model training): the Coupled Model Intercomparison Project,  
driven by the World Climate Research Program, is now in its 6th phase. Compared to previous model  
comparison projects, the CMIP6 project has a much better experimental design and more model  
development centres involved, as well as providing a much more significant amount of data. It provides



185 an excellent resource for studying current and future climate change (Eyring et al., 2016). The historical  
simulations of CMIP6 are designed to reproduce observed climate and climate change, constrained by  
radiative forcing. Its historical simulation spans between 1850 and 2014. In this study, we selected 125  
members from historical simulations of a large sample (a total of 507 members). These 125 members  
match better with the *in-situ* observations than the other (507-125) members. We selected the monthly  
190 downward shortwave radiation from 1955 to 2014 (see Table S1 in the Supplemental Material (SM)).  
Last access July 2022. Download at: <https://esgf-node.llnl.gov/search/cmip6>.

### 3 Methods

#### 3.1 Data Quality Control (QC) and homogenization

The SSR data homogenization method is only applied to the two inhomogenized *in-situ* observations  
195 datasets (GEBA and WRDC). The Quality Control (QC) and homogenization flowchart (Figure 1) is  
divided into three steps: 1. QC; 2. Homogenization; 3. Integration and consolidation.

##### 3.1.1 QC

The QC of SSR data includes the following steps:

- 200 1) Simple integration: integration of the GEBA (2445) and WRDC (1136) datasets removing stations  
with no data and leaving 2681 stations.
- 2) Removing duplicate stations: a. Stations with similar latitude and longitude. We consider two  
stations with totally identical latitude and longitude to be the same station; b. Stations less than 10km  
apart. We averaged the duplicate stations in this a and b case; c. Special duplicate stations: Stitching  
together data of the duplicate stations based on metadata from CMA.
- 205 3) Remove stations or years/months for which a climatic analysis cannot be established: we remove  
stations with records of less than ten years and values more than five times the standard deviation of the  
SSR anomalies.
- 210 4) Candidate stations (487) with a record length greater than 15 years in the period 1971-2000 are  
selected. We added stations (715) with more than 10 years of SSR records to increase the number of  
available stations for a better homogenization of the candidate stations (Figure 2).





### 3.1.2 Station series homogenization

This paper uses the RHtestV4 software package to test and adjust the SSR station data for homogeneity (<http://etcccdi.pacificclimate.org/software.shtml>) (Wang and Feng, 2013). The package is based on the empirical penalty functions PMF (Wang, 2008b) and PMT (Wang, 2008a; Wang et al., 2007) for the homogenization test. It takes into account the lag-1 autocorrelation of the time series. It embeds a multiple linear regression algorithm to significantly reduce the problem of an unbalanced distribution of pseudo-identification rates and test efficacy. Also, RHtestV4 uses the QM algorithm (Vincent et al., 2012; Wang et al., 2010) and Mean-Adjustments to adjust the identified change points.

The specific steps are as follows:

#### 1) Building the reference series

- a. We processed the data from all stations series (715) into the annual first differences (FD) series  $e_i$  (Eq. (1)) (Peterson et al., 1998).
- b. We calculated the correlation of the annual FD series between the series from the potential reference pool and the candidate stations.
- c. We calculated the distance between the potential reference pool stations and candidate stations.
- d. We selected potential stations according to the correlation coefficient ( $CC \geq 0.6$ ) between the series from potential reference pool and candidate stations. And the potential stations also satisfy the limits in distances ( $\leq 500\text{km}$ ) between the potential pool stations and candidate stations.
- e. We obtain the reference FD series ( $Re$ ) based on the  $m$  potential reference series ( $Pe_i$ ) and the CCs ( $c_i$ ) between the potential reference series ( $Pe_i$ ) and candidate stations series (Eq. (2)).
- f. The synthesized reference FD series ( $Re$ ) (Eq. (2)), plus the average of all potential reference series ( $\bar{R}$ ), yields the final annual reference series ( $R$ ) (Eq. (3)).

$$e_i = x_i - x_{i+1} \quad i=1, 2, \dots, n-1 \quad (1)$$

$$Re = \frac{\sum_{i=1}^m Pe_i * c_i^2}{\sum_{i=1}^m c_i^2} \quad (2)$$

$$R = Re + \bar{R} \quad (3)$$

$e_i$  Annual FD series,

$x_i$  Raw observational station SSR in the year  $i$ ,

$Re$  Final reference series,



$P e_i$  Potential reference series,

$c_i$  CC between the potential reference series and the candidate stations series.

## 2) Testing and adjusting the candidate series

The homogenization test algorithm used in this paper is the PMT. This method is a reference series-  
240 dependent test for a normalized candidate series. It assumes that the linear trend of the time series is zero  
and uses the degree of mean deviation at different points in the series to find change points. Furthermore,  
it eliminates the effect of different sample lengths on the test results. At the same time, the method  
introduces an empirical penalty factor, which effectively improves detection. We used the PMT to test  
the homogeneity of the candidate series based on the reference series established in 1). We then adjusted  
245 the statistically significant ( $p > 0.05$ ) changepoints obtained using the mean adjustment method ( $p > 0.05$ ).  
We homogenize the monthly series for 66 stations (see Figure S1 in the SM).

### 3.1.3 Integration and consolidation

As can be seen from Figure 1, the candidate stations (487) are relatively sparse. To better adapt deep  
learning methods for the dataset reconstruction later, we adjusted, added and integrated station series  
250 based on the results of homogenized data from other scholars: 1) We added stations with more than 10a  
overall (1955-2018) records but no more than 15a during the 1971-2000 period, and removed those  
stations that were clearly inhomogeneous (25) and some years of the station (3); 2) We subsequently  
integrate monthly SSR series for 116 stations based on the results of homogenization by other scholars  
(China (56), Japan (8), Europe (2) and Italy (50)). After the above steps, we end up with a homogenized  
255 dataset containing 944 stations (Figure 3). The details of the processing and classification are shown in  
Table S2 (see in the SM).

### 3.2 CNN model reconstruction methods

The CNN deep learning model network architecture uses a U-shaped structure similar to the U-net  
(Ronneberger et al., 2015). The advantage of using this model is: 1) both high and low-frequency  
260 information of the picture can be retained, and when reconstructing the SSR data, not only the grid point  
information close to the missing measurement point will be considered, but also information from more  
distant locations (which may be remotely correlated with that missing measurement point); 2) This makes  
the model convergence faster and more economical in terms of computational resources. The upper part  
of the U-shaped structure, which has no down samples or a low number of down samples, represents the



265 high-frequency information of the graph. These sections contain much of the detail in the graph and the  
relationships between similar grid points are conveyed by this section. The lower half of the U-shaped  
structure is down-sampled more often and represents the lower frequency information of the graph. The  
global radiation of a wide range of undulations is transmitted by it, and then the information at the various  
levels of the U-shaped structure is connected and transmitted through the skip connection, allowing the  
270 whole network to remember all the information of the picture very well. The model uses nearest  
neighbour upsampling in the decoding phase, the skip links will concatenate two feature maps and two  
masks as the feature and mask inputs for the next part of the convolution layer. The input to the last part  
of the convolution layer will contain the original input image concatenated with the holes and the original  
mask, allowing the model to replicate the non-hole pixels. The complex and variable nature of the sea-  
275 land boundary then has a significant impact on the reconstruction, when we reconstruct the global land  
SSR data. Therefore, we use partial convolution at the image boundaries with a suitable image padding,  
ensuring that the padding content at the image boundaries is not affected by values outside the image.  
The deep learning models' convolutional layers and loss functions have been described in SM.

We further reconstruct a long-term (1955-2018) global SSR anomalies dataset (SSRIH<sub>20CR</sub>) by using  
280 improved partial CNN deep learning methods based on a “perfect” dataset. CNN consists of three parts.  
A convolutional layer to reduce the number of weights by extracting local features, a pooling layer to  
reduce peakeeping and prevent overfitting, and a fully connected layer to output the desired result. In  
this paper, a modified CNN network is used to model the reconstruction of the SSR data, with the  
convolutional layer replaced by a partial convolution method and mask update. This method is the latest  
285 in image restoration effects and can restore irregular holes, an advantage over other image restoration  
methods that can only restore rectangular holes. Therefore, this paper uses the modified CNN model  
(Kadow et al., 2020) to recover the missing part of the global terrestrial SSR (except Antarctica). The  
specific reconstruction steps and processes are as in Figure 4.

### 3.2.1 Data pre-processing

290 The homogenized station data is converted to grid box anomalies using the Climate Anomalies Method  
(CAM) (Jones et al., 2001). CAM is a commonly used method for converting station anomaly data to  
gridded data. We divide all global areas into a  $5^\circ \times 5^\circ$  grid, after which we calculate the SSR anomalies  
(relative to 1923-2020) within the grid box by averaging the anomalies of all stations (at least 1 station



in it). If there are more than one site exists in the same grid box, the record length of this grid box is the  
295 total length of all sites in that grid box. Finally, we removed the values that were more than five times  
the standard deviation of the SSR anomaly time series after gridding. SSRs are all processed as daily  
average anomalies, i.e., monthly anomalies divided by 30 (each month is approximated as 30 days). We  
multiplied all the values by 30 again when the reconstruction is complete. The global land (except for  
Antarctica) distribution and coverage of SSRs after gridding are shown in Figure 5 a, b.

300 As seen in Figure 5a, the SSR is spatially sparsely distributed across South America and Africa. As  
shown in Figure 5b, SSR coverage increased yearly from 1950 until the mid-1970s, when it slowly  
decreased. In 2013, the coverage rate decreased sharply due to untimely data submission. Considering  
the SSR coverage above, we only kept the years (1955-2018) with data coverage of more than 8% of  
global land (except for Antarctica) areas.

305 Comparisons show that the ERA5 has high spatial resolution and relatively reliable performance in  
the temporal variations and long-term trends (Liang et al., 2022; Jiao et al., 2022). To obtain a higher  
data coverage and ensure that the AI model runs well, we used the ERA5 to fill the SSR of homogenized  
global gridded SSR in the Antarctic and ocean areas. However, if we use the SSR of ERA5 to directly  
fill the SSR of homogenized global gridded SSR ( $SSRIH_{grid}$ ) in the Antarctic and on the ocean areas,  
310 then the relatively weaker ocean SSR variations (variabilities, decadal changes, trends, etc.) from ERA5  
will inevitably introduce certain systematic biases in land SSR reconstruction due to the SSRs have the  
lower coverage on the land. Therefore, we designed an algorithm to avoid excessive diffusion of SSR  
system bias in terrestrial areas: we first calculated the ratios  $\gamma_i$  ( $i=1, 2, 3, \dots, n$ ) between the SSR from  
ERA5 and from  $SSRIH_{grid}$  on the land in all  $n$  years. For a single grid box, the  $\gamma_i$  have small changes  
315 and are regarded as a constant  $\gamma_{median}$  (Eq (4)), and the  $\gamma_{median}$  vary by latitude and longitude both on  
the marine and the land areas. We then extrapolated the  $\gamma_{median}$  for all the grid boxes along the land  
and sea boundaries. If there is no observation there, then the adjacent ocean ERA5 SSR is used to take  
its place after it is adjusted according to the differences between the SSR variations (represented by the  
linear trends) for the different underlying surfaces (Eq (5)).

$$\gamma_{median} = Median\left(\frac{OBS_{i_{land}}}{ERA5_{i_{land}}}\right), \quad (4)$$

$$OBS_{i_{O\&L}}(land) = ERA5_{i_{O\&L}}(Ocean) * \gamma_{median} * \frac{T_O}{T_L}, \quad (5)$$



$$i = 1, 2, 3, \dots, n$$

- 320  $\gamma_{\text{median}}$ : The median value of the ratios of OBS and ERA5 land SSR series,  
 $OBS_{i\_land}$ : Land SSR for the year  $i$  from SSRIH<sub>grid</sub> in a single grid,  
 $ERA5_{i\_land}$ : Land SSR for the year  $i$  from ERA5 in a single grid,  
 $OBS_{i\_O\&L}(land)$ : Land SSR along the sea-land boundary (land) for the year  $i$  from SSRIH<sub>grid</sub>,  
 $ERA5_{i\_O\&L}(Ocean)$ : Ocean SSR along the sea-land boundary for the year  $i$  from ERA5,
- 325  $T_O$ : Trend of ERA5 SSR on ocean areas in all  $n$  years,  
 $T_l$ : Trend of ERA5 SSR on areas in all  $n$  years.

### 3.2.2 AI Model reconstruction

We use a server (configured with processor Intel(R) Core (TM) i7-8700 CPU @ 3.20GHz 3.19 GHz,  
RAM 32G, 64-bit OS, GPU model 516.94, NVIDIA GeForce 1080T version, Python 3.9.12 64-bit,  
330 CUDA 10.1) for AI models training. The specific training steps are as follows:

- 1) A total of 768 missing value masks (monthly masks between 1955 and 2018) were prepared for training and validation using '1' for existing and '0' for missing values;
- 2) The 20CRv3/CMIP6 training set (monthly values between 1955 and 2015/2014) and missing value masks are fed into the 20CR-AI /CMIP6-AI model for training;
- 335 3) We perform 1,500,000 training sessions with an interval of 10,000 sessions for the training output model.

Afterwards, the two AI models are validated against the root mean squared error (RMSE)/CCs of the reconstructed SSRs ( $SSR_{20CR}/SSR_{CMIP6}$ ). The validation set SSRs, and the optimal number of training cycles is 1,100,000 (see Figure S2, Figure S3 and Figure S4 in the SM). The initial hyper-parameters of  
340 the model are set as follows; learning rate of  $2e-4$ , batch size of 16 and learning finetune of  $5e-5$ .

The training result models generated by the different AI models are obtained separately for the different training sets. The model is first used to reconstruct a reanalysis validation set with the same missing value mask as the original observation dataset. This is followed by a validation of the reconstruction against the original reanalysis dataset (calculation of CC and RMSE) to understand the  
345 discrepancies in the model reconstruction.



#### 4 Data homogenization and verification

We homogenized the original monthly stations/gridded SSR time series ( $SSRIH_{station} / SSRIH_{grid}$ ) using the method in section 3.1.2. We selected six continental regions, excluding Antarctica and the Arctic, from the eight continents of the world defined by Xu et al. (Xu et al., 2018) (Asia, Africa, South America, Europe, North America, Australia, Antarctica and the Arctic). The decreasing trend of the  $SSRIH_{grid}$  is consistent with the original gridded SSR series ( $SSRI_{grid}$ ) during 1955-1991 while the increasing trend during 1991-2018 is weaker. At the regional scale, the  $SSRIH_{grid}$  has a generally similar variation to the  $SSRI_{grid}$ , and the  $SSRIH_{grid}$  is usually more representative of climate change than  $SSRI_{grid}$  at individual stations.

Figure S5 (see in the SM) illustrates the long-term variations of global (Figure S5 (a) in the SM) and continental land SSR (Figure S5 (b) in the SM) from the  $SSRI_{grid}$  and  $SSRIH_{grid}$  (except for Antarctica) during 1955-2018. The most prominent change revolves around the adjustment around 1992: the SSR anomalies were systematically adjusted upward from 1987 to 1992, while the SSR anomalies were systematically adjusted downward from 1993 onwards. Thus, there is a significant decreasing trend for both global land  $SSRI_{grid}$  ( $-1.995 \pm 0.251$  W/m<sup>2</sup> per decade) and global land  $SSRIH_{grid}$  ( $-1.776 \pm 0.230$  W/m<sup>2</sup> per decade) (except for Antarctica) from 1955 to 1991. While the increasing trend of the global land  $SSRIH_{grid}$  from 1991 to 2018 is  $0.851 \pm 0.410$  W/m<sup>2</sup> per decade, slightly smaller than the increasing trend of the  $SSRI_{grid}$  ( $0.999 \pm 0.504$  W/m<sup>2</sup> per decade). It is worth noting that 1992 happened to be the second year of the eruption of Mount Pinatubo, and the homogenized SSR data integrated in this paper may be affected by this event. But overall, the homogenization also has limited effects on the global SSR variations from Figure S5 (see in the SM), which is consistent with the influence of data homogenization on a wide range of surface air temperatures (Brohan et al., 2006; Xu et al., 2013).

At the regional scale, the differences between the  $SSRIH_{grid}$  and  $SSRI_{grid}$  are more pronounced in Asia and Europe (see Figure S5(b) in the SM). Asia's homogenized SSR show that the regional average SSR has been declining significantly over the period 1958-90; this dimming trend mostly diminished over the period 1991-2005 and was replaced by a brightening trend in the recent decade. The  $SSRIH_{grid}$  in Asia is higher than the  $SSRI_{grid}$  from 1985 to 1990 and lower than the  $SSRI_{grid}$  from 2012 to 2015. The  $SSRIH_{grid}$  shows a more moderate short-term increase in Europe from 1960 to 1980. Note also that the Australian raw data prior to 1988 were artificially detrended because at the time the Australia Weather Service was



375 afraid that the instruments would drift. Therefore, they detrended them and unfortunately did not store  
the raw data, and the SSR evolution in Australia is artificial with no trend (Wild et al., 2005). In addition,  
the  $SSR_{station}$  and  $SSRH_{station}$  comparisons for all 66 stations are shown in Figure S1 (see in the SM).

## 5 AI reconstruction and comparison

### 5.1 Training of the AI model

380 We produce two (20CRv3 /CMIP6) separate training and validation sets: we select the 1th member  
data of the reanalysis data and the model data, respectively, as the validation set, and the remaining 79  
(124) ensemble members as the training sets, where each ensemble member included 732 (720) months  
of SSR data. Each validation set included 732 (720) samples, while the training sets contained 57828  
(89280) ensemble members. All the above data, including the *in-situ* observations, are then resampled to  
385 monthly anomalies of  $5^\circ \times 2.5^\circ$ .

We reconstruct the SSR of 20CRv3/CMIP6 with missing values based on 20CRv3 /CMIP6 datasets using  
the method in section 3.2 and obtain two reconstructions,  $SSR_{20CR}$  and  $SSR_{CMIP6}$ , respectively. The SSR  
of 20CRv3/CMIP6 with missing values uses the  $SSRH_{grid}$  mask between 1955 and 2015/2014. We  
compare the global land (except for Antarctica)/regional annual anomalies variation of  $SSR_{20CR}/SSR_{CMIP6}$ .  
390 The results show that  $SSR_{20CR}$  is significantly more consistent with the validation set than  $SSR_{CMIP6}$ .

Figure 6(a) shows that the RMSE/CC of the  $SSR_{20CR}$  ( $0.25 \text{ W/m}^2 / 0.97 \text{ W/m}^2$ ) are smaller/larger than  
those of  $SSR_{CMIP6}$  ( $0.52 \text{ W/m}^2 / 0.93 \text{ W/m}^2$ ) with the original 20CR/CMIP6 dataset. The 20CR-AI  
model has a better reconstruction ability for SSR at the global land (except for Antarctica) scale. The  
RMSEs of the  $SSR_{20CR}$  ( $SSR_{CMIP6}$ ) are 1.46 (2.41)  $\text{W/m}^2$ , 1.11 (1.83)  $\text{W/m}^2$ , 2.22 (2.60)  $\text{W/m}^2$  and 1.29  
395 (2.24)  $\text{W/m}^2$  in North America, Europe, Asia, and Northern Hemisphere, whereas these values are 1.12  
(1.77)  $\text{W/m}^2$ , 0.62 (1.60)  $\text{W/m}^2$ , 1.88 (1.84)  $\text{W/m}^2$  and 0.77 (1.68)  $\text{W/m}^2$  in South America, Africa,  
Australia, and Southern Hemisphere concerning the original 20CR/CMIP6 dataset, respectively. In  
other words, the RMSEs of the  $SSR_{20CR}$  are smaller than those of  $SSR_{CMIP6}$  for the original  
20CR/CMIP6 dataset except for Australia. In addition, the CCs of the  $SSR_{20CR}$  ( $SSR_{CMIP6}$ ) are 0.96 (0.83)  
400  $\text{W/m}^2$ , 0.96 (0.99)  $\text{W/m}^2$ , 0.89 (0.67)  $\text{W/m}^2$ , 0.93 (0.97)  $\text{W/m}^2$ , 0.94 (0.93)  $\text{W/m}^2$ , 0.94 (0.92)  $\text{W/m}^2$ , 0.94  
(0.88)  $\text{W/m}^2$  and 0.90 (0.82)  $\text{W/m}^2$  in North America, Europe, Asia, Northern Hemisphere, South  
America, Africa, Australia, and Southern Hemisphere with respect to the original 20CR /CMIP6



dataset, respectively. That is, the CCs of the  $SSR_{20CR}$  are larger than those of  $SSR_{CMIP6}$  to the original 20CR /CMIP6 dataset except for Europe.

405 Based on the above comparison, the higher uncertainty for CMIP6 model output possibly biases the CMIP6-AI method. Thus, the accuracy of the  $SSR_{20CR}$  is higher than that of the  $SSR_{CMIP6}$  at both global land (except for Antarctica) and regional scales. Therefore, we choose the reconstruction results of the 20CR-AI model as the final AI reconstruction dataset, and subsequent analysis in the following sections is only based on this dataset.

#### 410 5.2 Comparison of the spatial and temporal variation characteristics

We investigate the long-term trends and spatial and temporal variation of the  $SSRIH_{20CR}$ , compare the differences between the  $SSRIH_{20CR}$  and  $SSRIH_{grid}$ , and suggest: the area and magnitude of the high and low centres of the  $SSRIH_{20CR}$  are the same as those of the  $SSRIH_{grid}$ ; the results of the global land (except for Antarctica) reconstruction are consistent with "dimming and brightening"; the global dimming is 415 primarily dominated by decreasing trends in Asia, Europe Africa and North America, whereas Europe and North America are contributors to the increasing trends.

Figure 7 shows the spatial distribution of the  $SSRIH_{grid}$  and  $SSRIH_{20CR}$  for the three months (July 1960, July 1980, and July 2000). Figure S6 (see in the SM) displays the spatial distribution of annual  $SSRIH_{grid}$  and  $SSRIH_{20CR}$  from 1955 to 2018. Figure 7 also shows the area and the magnitude of the high and low 420 centres in the  $SSRIH_{20CR}$  are the same as in the  $SSRIH_{grid}$ . The  $SSRIH_{20CR}$  is mainly positive anomalies in Africa and the Eurasian continent in July 1960, especially in India and the Middle East. Afterwards, India showed a continuous and steady decline in SSR. This confirms the well-known phenomenon of global dimming over India (Wild et al., 2009; Soni et al., 2016; Soni et al., 2012; Padma Kumari et al., 2007; Kambezidis et al., 2012). In Australia, the  $SSRIH_{20CR}$  is dominated by negative anomalies in July 425 1980 and positive anomalies in July 1960 and July 2000. In Greenland, the  $SSRIH_{20CR}$  shows a large positive anomaly during three months. In northern Russia, there is a high value in July 2000. The reconstruction can better reflect the anomaly distribution of observation information, and the grid boxes with the missing values are infilled and reconstructed, which has high reliability.

Figure 8 illustrates global land (except for Antarctica) annual anomalies variation and long-term trend 430 of the  $SSRIH_{20CR}$  for the period of 1955-2018, 1955-1991 and 1991-2018. Also, we compare the differences between the  $SSRIH_{20CR}$  and  $SSRIH_{grid}$ . The minimum value of the  $SSRIH_{20CR}$  occurred in





1991 ( $-2.411 \text{ W/m}^2$ ). The decreasing trend of the  $\text{SSRIH}_{20\text{CR}}$  from 1955 to 1991 ( $-1.276 \pm 0.205 \text{ W/m}^2$  per decade) is slightly lower than that of the  $\text{SSRIH}_{\text{grid}}$  ( $-1.776 \pm 0.230 \text{ W/m}^2$  per decade). After that, the  $\text{SSRIH}_{20\text{CR}}$  turns to an increasing trend of  $0.697 \pm 0.359 \text{ W/m}^2$  per decade from 1991 to 2018. This suggests that the difference between  $\text{SSRIH}_{20\text{CR}}$  and  $\text{SSRIH}_{\text{grid}}$  may be caused by the results observed in limited data coverage (such as in Africa and North America) (Figure 9). After homogenization and reconstruction, the trend ( $-1.276 \text{ W/m}^2$  per decade) from 1955 to 1991 corresponds to an overall reduction of  $-4.6 \text{ W/m}^2$  over the dimming period, while that ( $0.697 \text{ W/m}^2$  per decade) from 1991 to 2018 correspond to an overall increase of  $2.0 \text{ W/m}^2$  over the brightening period. This is in amazing agreement with the  $-4 \text{ W/m}^2$  for the dimming period and the  $2 \text{ W/m}^2$  for the brightening period based on an overall surface energy budget assessment ((Wild, 2012) see their Figure 1). Also, similar conclusions (incomplete coverage of observational data lead to an underestimation of global warming trends) have been confirmed in global warming research (Gulev et al., 2021; Li et al., 2021).

Figure 9 demonstrates the long-term annual anomaly variations of the  $\text{SSRIH}_{20\text{CR}}$  in different regions and its results compared to the  $\text{SSRIH}_{\text{grid}}$ . The  $\text{SSRIH}_{20\text{CR}}$  shows a similar annual anomaly variation to the global land (except for Antarctica) average trend in North America and Asia, reaches a minimum in the late 1970s or early 1990s, and follows a moderate reversal. In Europe, the  $\text{SSRIH}_{20\text{CR}}$  shows a decrease ( $-2.180 \pm 1.866 \text{ W/m}^2$  per decade) between 1963 and 1978 before turning to brightening ( $1.081 \pm 0.312 \text{ W/m}^2$  per decade). In South America and Australia (Southern Hemisphere), the  $\text{SSRIH}_{20\text{CR}}$  shows no significant variation. In Africa, the  $\text{SSRIH}_{20\text{CR}}$  has a dimming trend ( $-1.506 \pm 0.496 \text{ W/m}^2$  per decade) from the 1950s to the 1990s, after which it remains levelled off ( $0.340 \pm 0.998 \text{ W/m}^2$  per decade). The  $\text{SSRIH}_{20\text{CR}}$  shows a decreasing trend ( $-1.457 \pm 0.246 \text{ W/m}^2$  per decade) until the 1990s in the Northern Hemisphere and a brightening ( $0.887 \pm 0.415 \text{ W/m}^2$  per decade) afterwards. The annual average anomaly variations in regions and globally show that Asia, Africa, Europe and North America are the four contributors to the global dimming, while Europe and North America are two major contributors to the “brightening”. This is in general agreement with the results obtained by previous machine learning (Yuan et al., 2021). In addition, the discrepancy between the  $\text{SSRIH}_{20\text{CR}}$  and  $\text{SSRIH}_{\text{grid}}$  is more significant in low-coverage areas (right) than in high-coverage regions (left). It is particularly pronounced before 1980 and in South America. This suggests that the limited surface observations are not representative of the continental variation in SSR.



To sum up, the AI reconstruction of this paper helps to decrease the uncertainties in SSR variations in both spatial scales. Further, it shows that there may be a sampling error in the variations of the global land (except for Antarctica) and regional SSR before reconstruction, leading to a systematic deviation in the long-term trend of global land (except for Antarctica) or regional SSR.

## 465 6 Data availability

Both the SSRIH<sub>grid</sub> (the homogenized monthly gridded SSR data over 1923-2020) and the SSRIH<sub>20CR</sub> (the monthly 20CR-AI model reconstructed SSR data for 1955-2018) are currently publicly available on the figshare website under DOI at <https://doi.org/10.6084/m9.figshare.21625079.v1> (Jiao and Li, 2023). These datasets are also available at <http://www.gwpu.net> for free.

## 470 7 Conclusion

In this study, we integrate global station observations based on the raw observational SSRs from GEBA and WRDC, combined with existing homogenized SSR datasets from other scholars. Also, we homogenize the globally distributed station data using the RHtestV4 software package. An improved CNN deep learning algorithm is subsequently used to reconstruct the SSR anomalies. Thus, a  
475 reconstructed SSR anomaly dataset, SSRIH<sub>20CR</sub>, is obtained based on training sets (20CRv3), for the years 1955-2018, with a resolution of 5°×2.5°. The main results are as follows:

- 1) The first integrated and homogenized global SSR monthly dataset is developed, which contains 944 stations in total and covers the longest periods (from the 1920s to recent years). A 5°×5° grid boxes version of the monthly SSR anomalies dataset is derived.
- 480 2) This paper develops 5°×2.5° full-coverage monthly land (except for Antarctica) SSR anomalies reconstructed datasets based on the above observations, using the 20CRv3 to train the AI model. Comparative validations /evaluations show that the SSRIH<sub>20CR</sub> provides a reliable benchmark for global SSR variations.
- 485 3) On average, the global annual SSR variations based on the SSRIH<sub>grid</sub> are not significantly different, except that the increasing (brightening) trend after 1991 is a little smaller for the latter. The short-term brightening SSR in Europe from the 1970s- to the 1980s disappear at the regional scale. At the same time, the brightening SSR after the 1990s in Asia slowed or postponed.



#### **Author contributions**

Boyang Jiao: Software, Data curation, Writing- Original draft preparation, Visualization, Investigation.

490 Yucheng Su: Software, Data curation.

Qingxiang Li: Methodology, Supervision, Conceptualization, Validation, Writing - Review and Editing.

Veronica Manara: Providing the homogenized Italian dataset, Writing - Review and Editing.

Martin Wild: Writing - Review and Editing.

#### **Competing interests**

495 At least one of the (co-)authors is a member of the editorial board of Earth System Science Data.

#### **Disclaimer**

Publisher's note: Copernicus Publications remains neutral about jurisdictional claims in published maps and institutional affiliations.

#### **Financial support**

500 This study is supported by the Natural Science Foundation of China (Grant: 41975105) and the National Key R&D Program of China (Grant: 2018YFC1507705; 2017YFC1502301). The Global Energy Balance Archive (GEBA) is co-funded by the Federal Office of Meteorology and Climatology MeteoSwiss within the framework of GCOS Switzerland. Global dimming and brightening research at ETH Zurich are supported by the Swiss National Science Foundation (Grant No. 200020 188601).

505 Veronica Manara was supported by the “Ministero dell'Università e della Ricerca” of Italy [grant FSE – REACT EU, DM 10/08/2021 n. 1062].



## Reference

- Aguiar, L. M., Pereira, B., David, M., Díaz, F., and Lauret, P.: Use of satellite data to improve solar radiation forecasting with Bayesian Artificial Neural Networks, *Solar Energy*, 122, 1309-1324, 510 doi:10.1016/j.solener.2015.10.041, 2015.
- Alexandersson, H.: A homogeneity test applied to precipitation data, *Journal of Climatology*, 6, 661-675, doi:10.1002/joc.3370060607, 1986.
- Bookstein, F. L.: Principal warps: Thin-plate splines and the decomposition of deformations, *IEEE Transactions on pattern analysis and machine intelligence*, 11, 567-585, doi:10.1109/34.24792, 1989.
- 515 Brohan, P., Kennedy, J. J., Harris, I., Tett, S. F. B., and Jones, P. D.: Uncertainty estimates in regional and global observed temperature changes: A new data set from 1850, *Journal of Geophysical Research: Atmospheres*, 111, doi:10.1029/2005JD006548, 2006.
- Cao, Y., Jiao, B., Lan, X., Tan, J., Yang, Y., Sun, W., Li, Z., Luo, J., and Li, Q.: Reconstruction of China global Merged Surface Temperature (CMST) based on an artificial intelligence approach 520 (submitted), *Environmental Science & Technology*, 2022.
- Collins, F. C.: A comparison of spatial interpolation techniques in temperature estimation, *The 3rd International Conference/Workshop on Integrating GIS and Environmental Modeling*, Santa Barbara, Santa Fe, NM; Santa Barbara, CA, 21-26 January 1996 of Conference.
- Craddock, J. M.: Methods of comparing annual rainfall records for climatic purposes, *Weather*, 34, 332- 525 346, doi:10.1002/j.1477-8696.1979.tb03465.x, 1979.
- Driemel, A., Augustine, J., Behrens, K., Colle, S., Cox, C., Cuevas-Agulló, E., Denn, F. M., Duprat, T., Fukuda, M., and Grobe, H.: Baseline Surface Radiation Network (BSRN): structure and data description (1992–2017), *Earth System Science Data*, 10, 1491-1501, doi:10.5194/essd-10-1491-2018, 2018.
- 530 Erxleben, J., Elder, K., and Davis, R.: Comparison of spatial interpolation methods for estimating snow distribution in the Colorado Rocky Mountains, *Hydrological Processes*, 16, 3627-3649, doi:10.1002/hyp.1239, 2002.
- Eyring, V., Bony, S., Meehl, G. A., Senior, C. A., Stevens, B., Stouffer, R. J., and Taylor, K. E.: Overview of the Coupled Model Intercomparison Project Phase 6 (CMIP6) experimental design and 535 organization, *Geoscientific Model Development*, 9, 1937-1958, doi:10.5194/gmd-9-1937-2016,



- 2016.
- Feng, F. and Wang, K.: Merging high-resolution satellite surface radiation data with meteorological sunshine duration observations over China from 1983 to 2017, *Remote Sensing*, 13, 602, doi:10.3390/rs13040602, 2021.
- 540 Fisher, N. I., Lewis, T., and Embleton, B. J.: Statistical analysis of spherical data, Cambridge university press, doi:10.1017/CBO9780511623059, 1993.
- Fukami, K., Fukagata, K., and Taira, K.: Machine-learning-based spatio-temporal super resolution reconstruction of turbulent flows, *Journal of Fluid Mechanics*, 909, doi:10.1017/jfm.2020.948, 2021.
- Gulev, S. K., Thorne, P. W., J. Ahn, F. J. D., Domingues, C. M., Gerland, S., Gong, D., Kaufman, D. S.,  
545 Nnamchi, H. C., Quaas, J., Rivera, J. A., Sathyendranath, S., Smith, S. L., Trewin, B., Shuckmann, K. v., and Vose, R. S.: In: *Climate Change 2021: The Physical Science Basis.*, *Climate Change 2021: The Physical Science Basis. Contribution of Working Group I to the Sixth Assessment Report of the Intergovernmental Panel on Climate Change*, in, edited by: [Masson-Delmotte, V., Zhai, P., Pirani, A., Connors, S. L., Péan, C., Berger, S., Caud, N., Chen, Y., Goldfarb, L., Gomis, M. I., Huang, M.,  
550 Leitzell, K., Lonnoy, E., Matthews, J. B. R., Maycock, T. K., Waterfield, T., Yelekçi, O., Yu, R., and (eds.)], B. Z., Cambridge University Press. 2021., 287–422. Cambridge University Press, 2021.
- Hersbach, H., Bell, B., Berrisford, P., Hirahara, S., Horányi, A., Muñoz-Sabater, J., Nicolas, J., Peubey, C., Radu, R., Schepers, D., Simmons, A., Soci, C., Abdalla, S., Abellan, X., Balsamo, G., Bechtold, P., Biavati, G., Bidlot, J. R., Bonavita, M., Chiara, G. D., Dahlgren, P., Dee, D., Diamantakis, M.,  
555 Dragani, R., Flemming, J., Forbes, R. G., Fuentes, M., Geer, A. J., Haimberger, L., Healy, S. B., Hogan, R. J., Holm, E. V., Janisková, M., Keeley, S. P. E., Laloyaux, P., Lopez, P., Lupu, C., Radnoti, G., Rosnay, P. d., Rozum, I., Vamborg, F., Villaume, S., and Thepaut, J.-N.: The ERA5 global reanalysis, *Quarterly Journal of the Royal Meteorological Society*, 146, 1999 - 2049, doi:10.1002/qj.3803, 2020.
- 560 Hoskins, B. J. and Valdes, P. J.: On the existence of storm-tracks, *Journal of Atmospheric Sciences*, 47, 1854-1864, doi:10.1175/1520-0469(1990)047<1854:OTEOST>2.0.CO;2, 1990.
- Huang, B., Yin, X., Menne, M. J., Vose, R., and Zhang, H.-M.: Improvements to the Land Surface Air Temperature Reconstruction in NOAA GlobalTemp: An Artificial Neural Network Approach, *Artificial Intelligence for the Earth Systems*, 1-35, doi:10.1175/AIES-D-22-0032.1, 2022.
- 565 Jiao, B. and Li, Q.: Global Integrated and Homogenized Solar surface Radiation Datasets,



- doi:10.6084/m9.figshare.21625079.v1, 2023.
- Jiao, B., Li, Q., Sun, W., and Martin, W.: Uncertainties in the global and continental surface solar radiation variations: inter-comparison of in-situ observations, reanalyses, and model simulations, *Climate Dynamics*, 1-18, doi:10.1007/s00382-022-06222-3, 2022.
- 570 Jones, P., Osborn, T., Briffa, K., Folland, C., Horton, E., Alexander, L., Parker, D., and Rayner, N.: Adjusting for sampling density in grid box land and ocean surface temperature time series, *Journal of Geophysical Research: Atmospheres*, 106, 3371-3380, doi:10.1029/2000JD900564, 2001.
- Ju, X., Tu, Q., and Li, Q.: Homogeneity test and reduction of monthly total solar radiation over China, *J Nanjing Inst Meteorol*, 29, 336-341, 2006.
- 575 Kadow, C., Hall, D. M., and Ulbrich, U.: Artificial intelligence reconstructs missing climate information, *Nature Geoscience*, 13, 408-413, doi:10.1038/s41561-020-0582-5, 2020.
- Kambezidis, H. D., Kaskaoutis, D. G., Kharol, S. K., Moorthy, K. K., Satheesh, S. K., Kalapureddy, M. C. R., Badarinath, K. V. S., Sharma, A. R., and Wild, M.: Multi-decadal variation of the net downward shortwave radiation over south Asia: The solar dimming effect, *Atmospheric*
- 580 *Environment*, 50, 360-372, 2012.
- Krige, D. G.: A statistical approach to some basic mine valuation problems on the Witwatersrand, *Journal of the Southern African Institute of Mining and Metallurgy*, 52, 119-139, doi:10.10520/AJA0038223X\_4792, 1951.
- Leirvik, T. and Yuan, M.: A machine learning technique for spatial interpolation of solar radiation
- 585 observations, *Earth and Space Science*, 8, e2020EA001527, doi:10.1029/2020EA001527, 2021.
- Li, Q., Sun, W., Yun, X., Huang, B., Dong, W., Wang, X. L., Zhai, P., and Jones, P.: An updated evaluation of the global mean land surface air temperature and surface temperature trends based on CLSAT and CMST, *Climate Dynamics*, 56, 635-650, doi: 10.1007/s00382-020-05502-0, 2021.
- Liang, H., Jiang, B., Liang, S., Peng, J., Li, S., Han, J., Yin, X., Cheng, J., Jia, K., and Liu, Q.: A global
- 590 long-term ocean surface daily/0.05° net radiation product from 1983–2020, *Scientific Data*, 9, 1-17, doi:10.1038/s41597-022-01419-x, 2022.
- Ma, Q., Wang, K., He, Y., Su, L., Wu, Q., Liu, H., and Zhang, Y.: Homogenized century-long surface incident solar radiation over Japan, *Earth System Science Data*, 14, 463-477, doi:10.5194/essd-14-463-2022, 2022.
- 595 Manara, V., Bassi, M., Brunetti, M., Cagnazzi, B., and Maugeri, M.: 1990–2016 surface solar radiation



- variability and trend over the Piedmont region (northwest Italy), *Theoretical and Applied Climatology*, 136, 849-862, doi:10.1007/s00704-018-2521-6, 2019.
- Manara, V., Brunetti, M., Celozzi, A., Maugeri, M., Sanchez-Lorenzo, A., and Wild, M.: Detection of dimming/brightening in Italy from homogenized all-sky and clear-sky surface solar radiation records and underlying causes (1959–2013), *Atmospheric Chemistry and Physics*, 16, 11145-11161, doi:10.5194/acp-16-11145-2016, 2016.
- Manara, V., Stocco, E., Brunetti, M., Diolaiuti, G. A., Fugazza, D., Pfeifroth, U., Senese, A., Trentmann, J., and Maugeri, M.: Comparison of Surface Solar Irradiance from Ground Observations and Satellite Data (1990–2016) over a Complex Orography Region (Piedmont—Northwest Italy), *Remote Sensing*, 12, 3882, 2020.
- Manara, V., Michele, B., M. M., S.-L. A., and Martin, W.: Homogenization of a surface solar radiation dataset over Italy, *AIP Conference Proceedings*, 22 February 2017, doi:org/10.1063/1.4975544, 2017.
- Mlawer, E. J., Taubman, S. J., Brown, P. D., Iacono, M. J., and Clough, S. A.: Radiative transfer for inhomogeneous atmospheres: RRTM, a validated correlated-k model for the longwave, *Journal of Geophysical Research: Atmospheres*, 102, 16663-16682, <https://doi.org/10.1029/97JD00237>, 1997.
- Padma Kumari, B., Londhe, A. L., Daniel, S., and Jadhav, D. B.: Observational evidence of solar dimming: Offsetting surface warming over India, *Geophysical Research Letters*, 34, <https://doi.org/10.1029/2007GL031133>, 2007.
- Peixoto, J. P., Oort, A. H., and Lorenz, E. N.: *Physics of climate*, Springer 1992.
- Peterson, T. C., Karl, T. R., Jamason, P. F., Knight, R., and Easterling, D. R.: First difference method: Maximizing station density for the calculation of long-term global temperature change, *Journal of Geophysical Research: Atmospheres*, 103, 25967-25974, doi:10.1029/98JD01168, 1998.
- Pfeifroth, U., Sanchez-Lorenzo, A., Manara, V., Trentmann, J., and Hollmann, R.: Trends and Variability of Surface Solar Radiation in Europe Based On Surface- and Satellite-Based Data Records, *Journal of Geophysical Research: Atmospheres*, 123, 1735-1754, doi: 10.1002/2017JD027418, 2018.
- Ronneberger, O., Fischer, P., and Brox, T.: U-net: Convolutional networks for biomedical image segmentation, *International Conference on Medical image computing and computer-assisted intervention*, 234-241, doi:10.48550/arXiv.1505.04597,
- Sanchez-Lorenzo, A., Calbó, J., and Wild, M.: Global and diffuse solar radiation in Spain: Building a



- homogeneous dataset and assessing their trends, *Global and Planetary Change*, 100, 343-352, doi:10.1016/j.gloplacha.2012.11.010, 2013a.
- Sanchez-Lorenzo, A., Wild, M., and Trentmann, J.: Validation and stability assessment of the monthly mean CM SAF surface solar radiation dataset over Europe against a homogenized surface dataset (1983–2005), *Remote sensing of environment*, 134, 355-366, doi:10.1016/j.rse.2013.03.012, 2013b.
- 630 Sanchez-Lorenzo, A., Wild, M., Brunetti, M., Guijarro, J. A., Hakuba, M. Z., Calbó, J., Mystakidis, S., and Bartok, B.: Reassessment and update of long-term trends in downward surface shortwave radiation over Europe (1939–2012), *Journal of Geophysical Research: Atmospheres*, 120, 9555-9569, doi:10.1002/2015JD023321, 2015.
- 635 Scudiero, E., Corwin, D. L., Morari, F., Anderson, R. G., and Skaggs, T. H.: Spatial interpolation quality assessment for soil sensor transect datasets, *Computers and Electronics in Agriculture*, 123, 74-79, doi:10.1016/j.compag.2016.02.016, 2016.
- Shepard, D.: A two-dimensional interpolation function for irregularly-spaced data, *Proceedings of the 1968 23rd ACM national conference*, 517-524, doi:10.1145/800186.810616,
- 640 Slivinski, L. C., Compo, G. P., Whitaker, J. S., Sardeshmukh, P. D., Giese, B. S., McColl, C., Allan, R., Yin, X., Vose, R., and Titchner, H.: Towards a more reliable historical reanalysis: Improvements for version 3 of the Twentieth Century Reanalysis system, *Quarterly Journal of the Royal Meteorological Society*, 145, 2876-2908, doi:10.1002/qj.3598, 2019.
- Soni, V. K., Pandithurai, G., and Pai, D. S.: Evaluation of long-term changes of solar radiation in India, *International Journal of Climatology*, 32, 540-551, <https://doi.org/10.1002/joc.2294>, 2012.
- 645 Soni, V. K., Pandithurai, G., and Pai, D. S.: Is there a transition of solar radiation from dimming to brightening over India, *Atmospheric Research*, 169, 209-224, 2016.
- Tang, W., Yang, K., Qin, J., Li, X., and Niu, X.: A 16-year dataset (2000–2015) of high-resolution (3 h, 10 km) global surface solar radiation, *Earth System Science Data*, 11, 1905-1915, doi:10.5194/essd-11-1905-2019, 2019.
- 650 Tang, W., Qin, J., Yang, K., Liu, S., Lu, N., and Niu, X.: Retrieving high-resolution surface solar radiation with cloud parameters derived by combining MODIS and MTSAT data, *Atmospheric Chemistry and Physics*, 16, 2543-2557, doi:10.5194/acp-16-2543-2016, 2016.
- Trenberth, K. E. and Fasullo, J. T.: Regional energy and water cycles: Transports from ocean to land, *Journal of Climate*, 26, 7837-7851, doi:10.1175/JCLI-D-13-00008.1, 2013.
- 655





- Tsvetkov, A., Wilcox, S., Renne, D., and Pulscak, M.: International solar resource data at the World Radiation Data Center, American Solar Energy Society, Boulder, CO (United States), 1995.
- Vincent, L. A., Wang, X. L., Milewska, E. J., Wan, H., Yang, F., and Swail, V.: A second generation of homogenized Canadian monthly surface air temperature for climate trend analysis, *Journal of Geophysical Research: Atmospheres*, 117, doi:10.1029/2012JD017859, 2012.
- 660 Wang, K.: Measurement biases explain discrepancies between the observed and simulated decadal variability of surface incident solar radiation, *Scientific reports*, 4, 1-7, doi:0.1038/srep06144 2014.
- Wang, K., Ma, Q., Li, Z., and Wang, J.: Decadal variability of surface incident solar radiation over China: Observations, satellite retrievals, and reanalyses, *Journal of Geophysical Research: Atmospheres*, 665 120, 6500-6514, doi:10.1002/2015JD023420, 2015.
- Wang, X. L.: Accounting for autocorrelation in detecting mean shifts in climate data series using the penalized maximal t or F test, *Journal of applied meteorology and climatology*, 47, 2423-2444, doi:10.1175/2008JAMC1741.1, 2008a.
- Wang, X. L.: Penalized maximal F test for detecting undocumented mean shift without trend change, 670 *Journal of Atmospheric and Oceanic Technology*, 25, 368-384, doi:10.1175/2007JTECHA982.1, 2008b.
- Wang, X. L. and Feng, Y.: RHtestsV4 user manual, Climate Research Division, Atmospheric Science and Technology Directorate, Science and Technology Branch, Environment Canada, 28, 2013.
- Wang, X. L., Wen, Q. H., and Wu, Y.: Penalized maximal t test for detecting undocumented mean change 675 in climate data series, *Journal of Applied Meteorology and Climatology*, 46, 916-931, doi:10.1175/JAM2504.1, 2007.
- Wang, X. L., Chen, H., Wu, Y., Feng, Y., and Pu, Q.: New techniques for the detection and adjustment of shifts in daily precipitation data series, *Journal of Applied Meteorology and Climatology*, 49, 2416-2436, doi:10.1175/2010JAMC2376.1, 2010.
- 680 Wang, Y. and Wild, M.: A new look at solar dimming and brightening in China, *Geophysical Research Letters*, 43, 11,777-711,785, doi:10.1002/2016GL071009, 2016.
- Wild, M.: Enlightening global dimming and brightening, *Bulletin of the American Meteorological Society*, 93, 27-37, doi:10.1175/BAMS-D-11-00074.1, 2012.
- Wild, M., Trüssel, B., Ohmura, A., Long, C. N., König-Langlo, G., Dutton, E. G., and Tsvetkov, A.: 685 Global dimming and brightening: An update beyond 2000, *Journal of Geophysical Research:*



- Atmospheres, 114, <https://doi.org/10.1029/2008JD011382>, 2009.
- Wild, M., Ohmura, A., Schär, C., Müller, G., Folini, D., Schwarz, M., Hakuba, M. Z., and Sanchez-Lorenzo, A.: The Global Energy Balance Archive (GEBA) version 2017: A database for worldwide measured surface energy fluxes, *Earth System Science Data*, 9, 601-613, doi:10.5194/essd-9-601-690 2017, 2017.
- Wild, M., Gilgen, H., Roesch, A., Ohmura, A., Long, C. N., Dutton, E. G., Forgan, B., Kallis, A., Russak, V., and Tsvetkov, A.: From dimming to brightening: Decadal changes in solar radiation at Earth's surface, *Science*, 308, 847-850, doi:10.1126/science.1103215, 2005.
- Xu, W., Li, Q., Wang, X. L., Yang, S., Cao, L., and Feng, Y.: Homogenization of Chinese daily surface air temperatures and analysis of trends in the extreme temperature indices, *Journal of Geophysical Research: Atmospheres*, 118, 9708-9720, doi:10.1002/jgrd.50791, 2013.
- Xu, W., Li, Q., Jones, P., Wang, X. L., Trewin, B., Yang, S., Zhu, C., Zhai, P., Wang, J., and Vincent, L.: A new integrated and homogenized global monthly land surface air temperature dataset for the period since 1900, *Climate Dynamics*, 50, 2513-2536, doi:10.1007/s00382-017-3755-1, 2018.
- 700 Yang, L., Zhang, X., Liang, S., Yao, Y., Jia, K., and Jia, A.: Estimating surface downward shortwave radiation over China based on the gradient boosting decision tree method, *Remote Sensing*, 10, 185, doi:10.3390/rs10020185, 2018a.
- Yang, S.: Chinese Monthly homogenized surface solar radiation datasets (V 1.0), 2016.
- Yang, S., Wang, X. L., and Wild, M.: Homogenization and trend analysis of the 1958–2016 in situ surface solar radiation records in China, *Journal of Climate*, 31, 4529-4541, doi:10.1175/JCLI-D-17-0891.1, 705 2018b.
- You, Q., Sanchez-Lorenzo, A., Wild, M., Folini, D., Fraedrich, K., Ren, G., and Kang, S.: Decadal variation of surface solar radiation in the Tibetan Plateau from observations, reanalysis and model simulations, *Climate dynamics*, 40, 2073-2086, doi:10.1007/s00382-012-1383-3, 2013.
- 710 Yuan, M., Leirvik, T., and Wild, M.: Global trends in downward surface solar radiation from spatial interpolated ground observations during 1961–2019, *Journal of Climate*, 34, 9501-9521, doi:10.1175/JCLI-D-21-0165.1, 2021.



### Captions of tables and Figures

715 Table 1: List of information on the various types of data used in this paper.

Figure 1: Flowchart of quality control (QC) (first step), homogenization (second step) and integration (third step).

720 Figure 2: Spatial distribution of candidate stations (“\*\*”) and added stations (“+”). The different colour bars represent the length of the station record in months (Units: Month).

Figure 3: Spatial distribution of stations after homogenization (Units: Month), different colours represent the length of station records in months

725

Figure 4: Flowchart of AI reconstruction.

730 Figure 5: (a) Spatial distribution of 5°x5° grid boxes (SSRIHgrid) obtained interpolating the homogenized global land (except for Antarctica) SSR series. The different colours represent the length (the sum of all records) of the station record, Units: Year. (b) Grid box coverage for the homogenized global land (except for Antarctica) SSR (SSRIHgrid) except for Antarctica.

Figure 6: Reconstruction capabilities of the AI model.

735 Figure 7: Spatial distribution of the SSRIHgrid (a1-3) and SSRIH<sub>20CR</sub> (b1-3) in typical months. 1-3 is July 1960, July 1980, and July 2000, respectively.

Figure 8: Global land (except for Antarctica) time series of the annual anomaly variations SSR (relative to 1971-2000) before/after reconstruction.

740

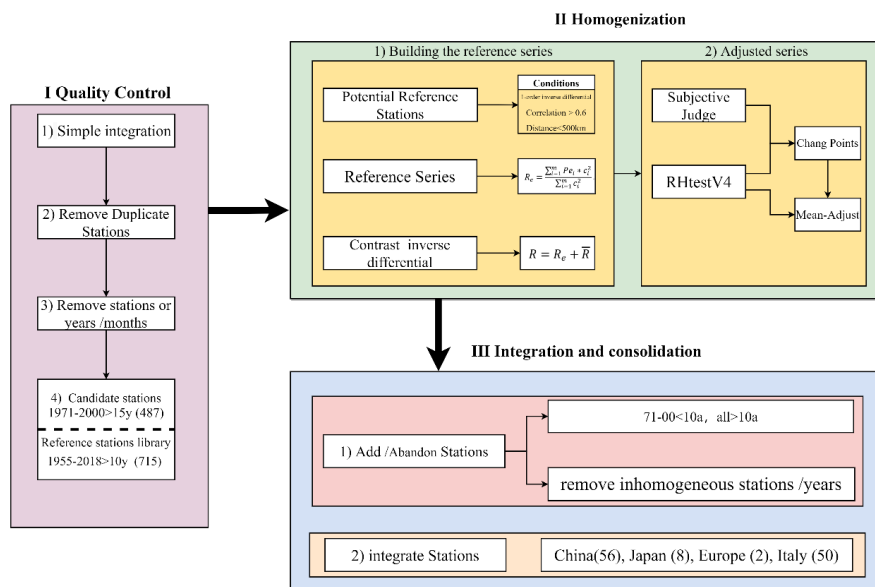
Figure 9: Same as Figure 8, but for regional annual anomaly variations.



**Table 1: List of information on the various types of data used in this paper**

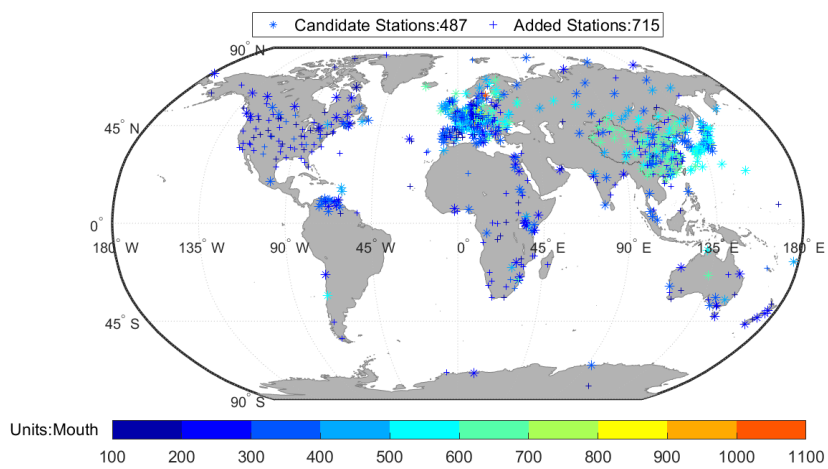
	Abbreviation	Resolution	Time	Reference
<i>In-situ</i> -Raw	GEBA (Station)	Monthly	1922-2020	(Wild et al., 2017)
	WRDC (Station)	Monthly	1964-2017	(Tsvetkov et al., 1995)
<i>In-situ</i> -Homo	China (Station)	Monthly	1950-2016	(Yang et al., 2018b)
	Japan (Station)	Monthly	1870-2015	(Ma et al., 2022)
	Europe (Station)	Monthly	1922-2012	(Sanchez-Lorenzo et al., 2015)
	Italy (Station)	Monthly	1959-2016	(Manara et al., 2016; Manara et al., 2019)
Reanalysis / Model	ERA5 (Grid)	Monthly/ 0.25°×0.25°	1950-2020	(Hersbach et al., 2020)
	20CRv3 (Grid)	Monthly/ (0.7°×0.7°/1°×1°)	1940-2015	(Slivinski et al., 2019)
	CMIP6 (Grid)	Monthly/-	1940-2014	(Eyring et al., 2016)

745

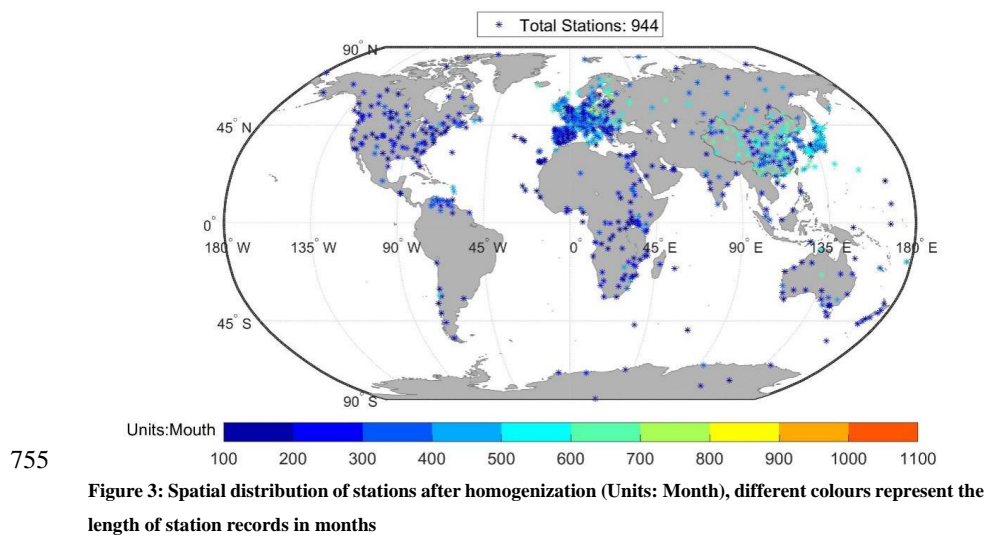


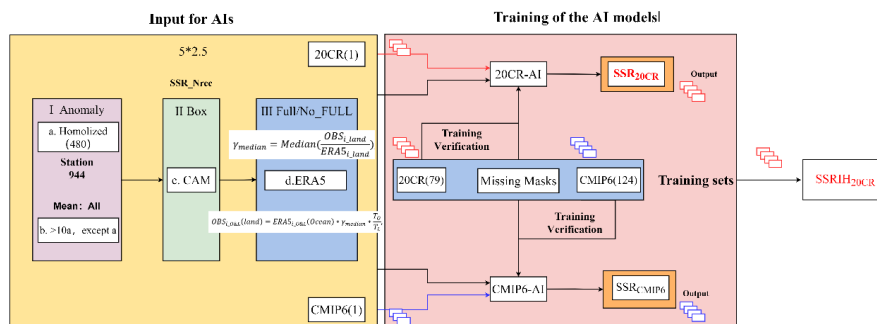
**Figure 1: Flowchart of quality control (QC) (first step), homogenization (second step) and integration (third step).**

750



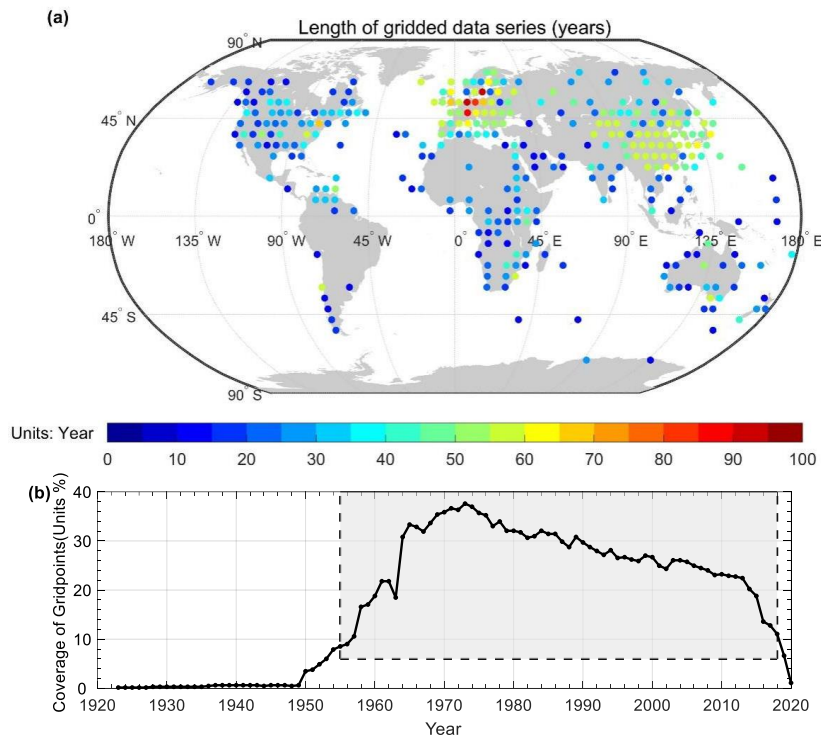
**Figure 2: Spatial distribution of candidate stations (“\*”) and added stations (“+”). The different colour bars represent the length of the station record in months (Units: Month).**



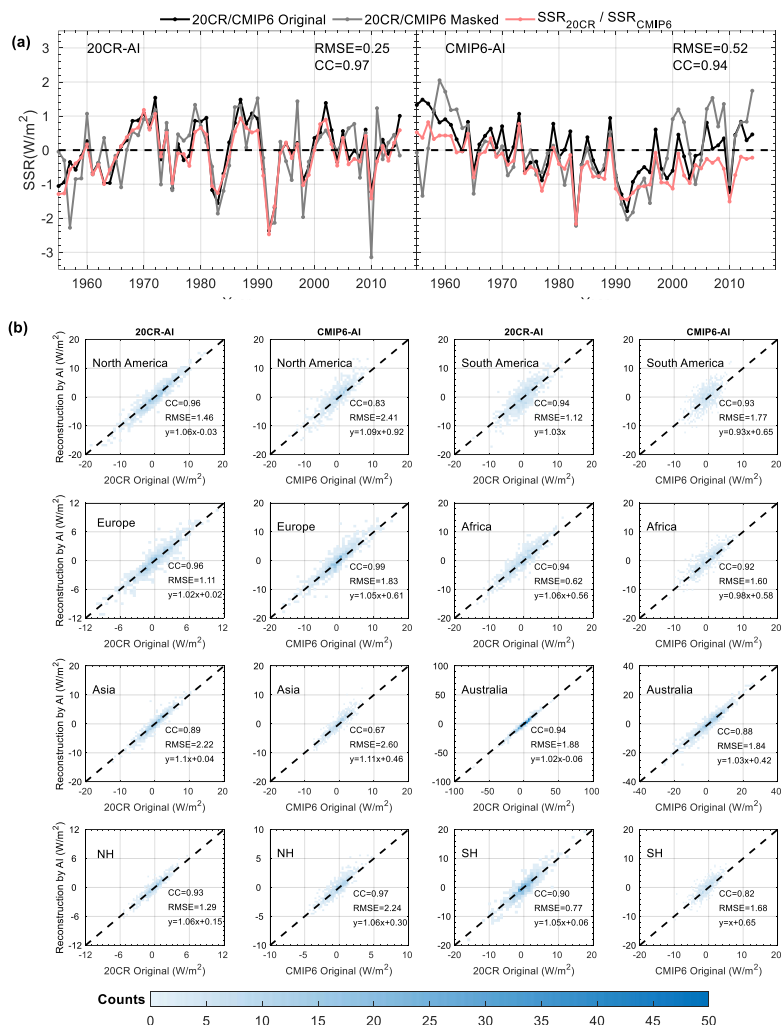


760 **Figure 4: Flowchart of AI reconstruction.**

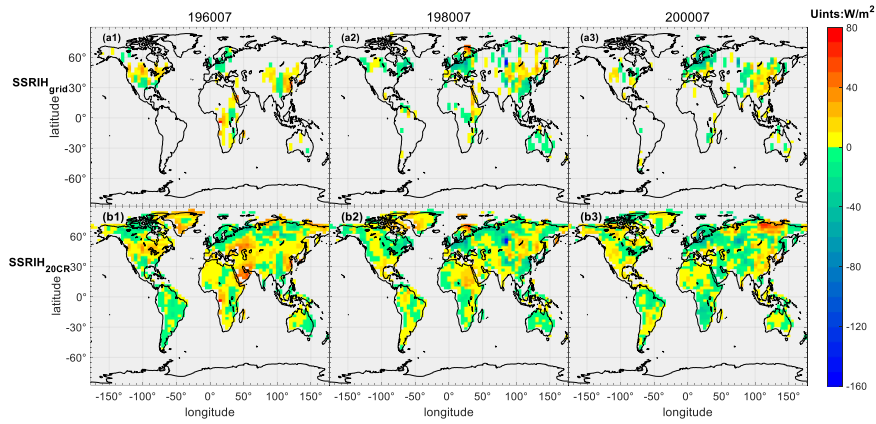




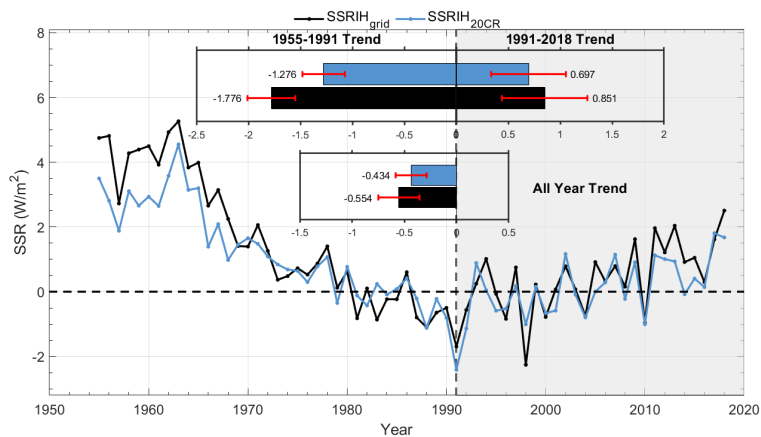
765 **Figure 5: (a) Spatial distribution of  $5^{\circ} \times 5^{\circ}$  grid boxes ( $SSRIH_{grid}$ ) obtained interpolating the homogenized global land (except for Antarctica) SSR series. The different colours represent the length (the sum of all records) of the station record, Units: Year. (b) Grid box coverage for the homogenized global land (except for Antarctica) SSR ( $SSRIH_{grid}$ ) except for Antarctica.**



770 **Figure 6: Reconstruction capabilities of the AI model. (a) Global land (except for Antarctica) means time-**  
**series analysis and AI model reconstruction evaluation. The red line is the SSR of the reconstruction based**  
**on the 20CR-AI /CMIP6-AI model ( $SSR_{20CR} / SSR_{CMIP6}$ ); The grey line is the masked datasets with missing**  
**values of the  $SSR_{IH_{grid}}$ . The solid black line is the 20CR and CMIP6 validation set (the SSR from the 1th**  
**member of 20CRv3 /CMIP6). (b) Comparisons of the  $SSR_{20CR}$  (columns 1, 3)/ $SSR_{CMIP6}$  (columns 2, 4)**  
**with the SSR from the 20CR and CMIP6 validation set. Colour bars represent counts with the same values for**  
 775 **both. Figures also show the  $SSR_{20CR}$  ( $SSR_{CMIP6}$ ) correlation coefficient (CC), root mean squared error (RMSE)**  
**and fitting equation compared to the original dataset in different regions.**



780 **Figure 7: Spatial distribution of the  $SSRIH_{grid}$  (a1-3) and  $SSRIH_{20CR}$  (b1-3) in typical months. 1-3 is July 1960, July 1980, and July 2000, respectively.**



785 **Figure 8:** Global land (except for Antarctica) annual SSR anomaly variations (relative to 1971-2000)  
before/after reconstruction. The Black solid line represents the SSRIH<sub>grid</sub> annual anomalies. The solid blue  
line represents the SSRIH<sub>20CR</sub> annual anomalies. The histograms represent the decadal trends of the  
SSRIH<sub>grid</sub> /SSRIH<sub>20CR</sub> (unit: W/m<sup>2</sup> per decade) and their 95% uncertainty range from 1955 to 1991, 1991-  
2018 and 1955-2018.

790

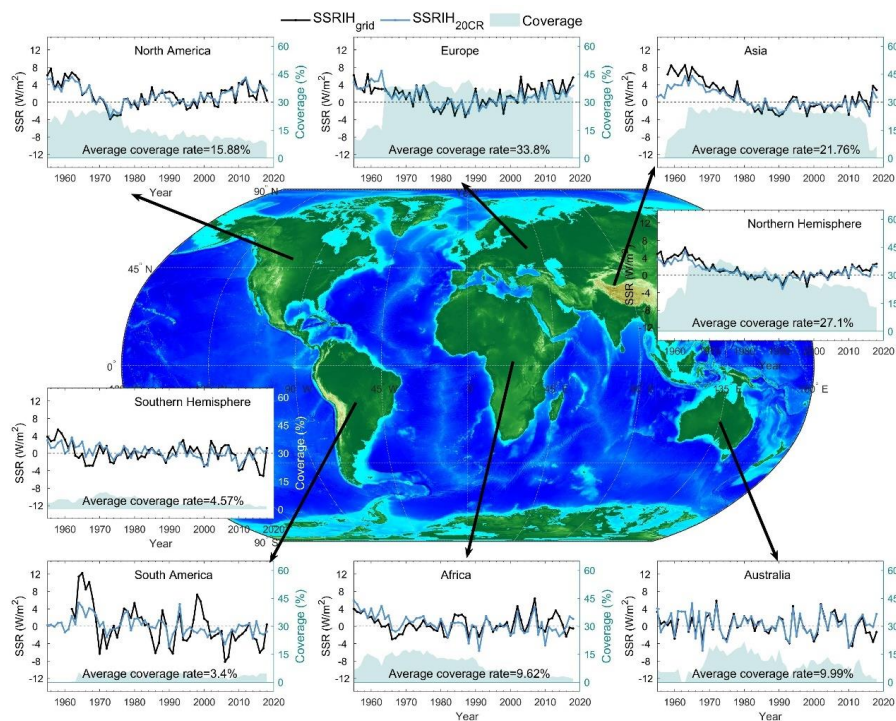


**Figure 9:** Same as Figure 8, but for regional annual anomaly variations. The green colour filling diagram represents the variation in grid box coverage (before reconstruction).